

Article

# Non-Hydrostatic Galerkin Model with Weighted Average Pressure Profile

Lucas Calvo <sup>1,2,\*</sup>, Diana De Padova <sup>3</sup>  and Michele Mossa <sup>3</sup> 

<sup>1</sup> Center for Hydraulic and Hydrotechnical Research, Technological University of Panama, Panama 0819-07289, Panama

<sup>2</sup> National Research System, SNI-SENACYT, Panama 0816-02852, Panama

<sup>3</sup> Department of Civil, Environmental, Land, Building Engineering and Chemistry (DICATECh), Polytechnic University of Bari, Via E. Orabona 4, 70125 Bari, Italy; diana.depadova@poliba.it (D.D.P.); michele.mossa@poliba.it (M.M.)

\* Correspondence: lucas.calvo@utp.ac.pa

**Abstract:** This work develops a novel two-dimensional, depth-integrated, non-hydrostatic model for wave propagation simulation using a weighted average non-hydrostatic pressure profile. The model is constructed by modifying an existing non-hydrostatic discontinuous/continuous Galerkin finite-element model with a linear, vertical, non-hydrostatic pressure profile. Using a weighted average linear/quadratic non-hydrostatic pressure profile has been shown to increase the performance of earlier models. The results suggest that implementing a weighted average non-hydrostatic pressure profile, in conjunction with a calculated or optimized  $\Theta$  weight parameter, improves the dispersion characteristics of depth-integrated, non-hydrostatic models in shallow and intermediate water depths. A series of analytical solutions and data from previous laboratory experiments verify and validate the model.

**Keywords:** depth-integrated; discontinuous Galerkin finite-element method; linear/quadratic non-hydrostatic pressure profile; wave propagation



Academic Editors: Ali Cemal Benim, Jeffrey S. Marshall, Sergey A. Karabasov and Dimitris Drikakis

Received: 20 January 2025

Revised: 5 March 2025

Accepted: 6 March 2025

Published: 13 March 2025

**Citation:** Calvo, L.; De Padova, D.; Mossa, M. Non-Hydrostatic Galerkin Model with Weighted Average Pressure Profile. *Computation* **2025**, *13*, 73. <https://doi.org/10.3390/computation13030073>

**Copyright:** © 2025 by the authors. Licensee MDPI, Basel, Switzerland. This article is an open access article distributed under the terms and conditions of the Creative Commons Attribution (CC BY) license (<https://creativecommons.org/licenses/by/4.0/>).

## 1. Introduction

Over the past few decades, the importance of research into how waves travel along the shoreline has grown. This is mostly because of the occurrence of many coastal disasters, some of which have been exacerbated by rising sea levels. In the field of wave propagation simulation, depth-integrated models employing Boussinesq-type equations have historically been the prevailing approach. Nevertheless, the high-order partial-derivative terms present in these equations pose significant challenges during discretization, leading to numerical instabilities and a substantial computational burden. Furthermore, the fundamental equations of the Boussinesq type are derived under the assumption of negligible rotation and viscosity, a premise that may not always be valid

Since their initial formulation by Casulli and Stelling [1] and Stansby and Zhou [2], shallow water models with non-hydrostatic pressure have demonstrated their ability to effectively model nonlinear and dispersive waves. The vertical momentum of water waves is addressed in these simulations by incorporating a non-hydrostatic pressure component into the Reynolds-averaged Navier–Stokes equations. Non-hydrostatic models for water waves are of two types: single-layer or multi-layer. Single-layer models are 2D depth-integrated, non-hydrostatic models, while multi-layer models are 3D non-hydrostatic models. Researchers have shown that non-hydrostatic models can predict water waves with single or multiple layers [3–6].

In their study, Calvo et al. [7] presented a depth-integrated, non-hydrostatic model for wave propagation, breaking, and runup simulation in a finite-element setting. As with all preceding non-hydrostatic models, it employs a linear vertical profile for the non-hydrostatic pressure. Linearization of the vertical momentum equations has led to the recognition that depth-integrated, non-hydrostatic models are relevant solely to intermediate water depths and weakly nonlinear conditions [8].

In recent research, emphasis has been placed on enhancing the order of the non-hydrostatic pressure interpolation to a quadratic profile. As demonstrated in research by Jeschke et al. [9] and Wang et al. [10], this modification has shown benefits in terms of dispersion, particularly in shallow-water settings. However, its efficacy is less pronounced in intermediate water depths [11,12].

The main objective of this research is to develop a new depth-integrated, non-hydrostatic model for wave propagation, using a weighted average pressure profile that can exhibit improved dispersion characteristics in shallow and intermediate water depths.

To achieve these goals, we modified the previous non-hydrostatic, discontinuous/continuous Galerkin finite-element model proposed by Calvo et al. [7]. This model’s use of unstructured meshes enables local refinement and facilitates the management of complex boundaries, which can be a significant advantage. Furthermore, linear quadrilateral finite elements require fewer nodal variables than linear triangular elements in a discontinuous Galerkin framework and possess a higher order of interpolation. The aforementioned characteristics suggest that the novel method may serve as a compelling alternative for the modeling of shallow and intermediate water waves. This approach could also circumvent the numerical challenges associated with Boussinesq-type models and the augmented computational expenses that result from a more extensive array of vertical layers in a multi-layer, non-hydrostatic model.

## 2. Description of the Model

The suggested model begins with the non-hydrostatic discontinuous/continuous Galerkin finite-element model described by Calvo et al. [7], with the model being built with a mix of discontinuous and continuous Galerkin methods. The depth-integrated, non-hydrostatic equations are divided into hydrostatic and non-hydrostatic components. The hydrostatic component is equivalent to the depth-integrated shallow-water equations. It is resolved through the implementation of a discontinuous Galerkin method, which facilitates the simulation of discontinuous regimes, wave breaking, and runup. The non-hydrostatic component yielded a Poisson-type equation, where the non-hydrostatic pressure was solved by a continuous Galerkin method for simulation of wave propagation and shoaling. The model employs linear quadrilateral elements to calculate horizontal velocities, water surface elevations, and non-hydrostatic pressures. This approach enables local refinement and incorporation of arbitrary boundaries.

The equations that describe depth-integrated, non-hydrostatic flow, written in a way that keeps track of mass and momentum conservation, are expressed as follows:

$$\frac{\partial HU}{\partial t} + \frac{\partial HUU}{\partial x} + \frac{\partial HUV}{\partial y} = -gH \frac{\partial \xi}{\partial x} - \frac{gn^2 U \sqrt{U^2 + V^2}}{H^{\frac{1}{3}}} - \frac{H}{2\rho} \frac{\partial q_b}{\partial x} - \frac{q_b}{2\rho} \frac{\partial(\xi - h)}{\partial x} \tag{1}$$

$$\frac{\partial HV}{\partial t} + \frac{\partial HUV}{\partial x} + \frac{\partial HVV}{\partial y} = -gH \frac{\partial \xi}{\partial y} - \frac{gn^2 V \sqrt{U^2 + V^2}}{H^{\frac{1}{3}}} - \frac{H}{2\rho} \frac{\partial q_b}{\partial y} - \frac{q_b}{2\rho} \frac{\partial(\xi - h)}{\partial y} \tag{2}$$

$$\frac{\partial H}{\partial t} + \frac{\partial UH}{\partial x} + \frac{\partial VH}{\partial y} = 0 \tag{3}$$

$$\frac{\partial W}{\partial t} = \frac{q_b}{\rho H} \tag{4}$$

In the context of the non-hydrostatic wave equations above, the following variables are relevant:  $U$ ,  $V$ , and  $W$  represent the depth-averaged velocity components in the  $x$ ,  $y$ , and  $z$  directions, respectively. The water density is denoted by  $\rho$ . The Manning roughness coefficient ( $n$ ) and the gravitational acceleration ( $g$ ) are also of significance. The flow depth, denoted by  $H$ , is expressed as a function of the surface elevation ( $\zeta$ ) measured from the level of still water and the water depth ( $h$ ) measured from the same reference point. Assuming a linear variation in the vertical direction for non-hydrostatic pressures and vertical velocities, the following hypotheses are proposed: the non-hydrostatic pressure on the surface is zero, and that at the bottom is  $q_b$ ; the impacts of turbulence, atmospheric pressure, baroclinic pressure gradient, and Coriolis force are not considered, but the incorporation of these effects into a simulation is totally feasible; and the average vertical velocity ( $W$ ) is taken as  $(w_\zeta + w_b)/2$ , where  $w_\zeta$  and  $w_b$  are the vertical velocities at the surface and at the bottom, respectively. Due to the linearization of the vertical momentum (Equation (4)), the depth-integrated, non-hydrostatic formulations are only applicable to weakly nonlinear scenarios.

The solution is initiated through the application of a discontinuous Galerkin method, whereby the horizontal momentum equations (Equations (1) and (2)) are solved without the non-hydrostatic pressure terms. These horizontal momentum equations, when combined with the mass conservation equation (Equation (3)) can be expressed in the conservative form of Equation (5):

$$\frac{\partial \mathbf{U}}{\partial t} + \nabla \times \mathbf{F}(\mathbf{U}) = \frac{\partial \mathbf{U}}{\partial t} + \frac{\partial \mathbf{E}(\mathbf{U})}{\partial x} + \frac{\partial \mathbf{G}(\mathbf{U})}{\partial y} = \mathbf{S}(\mathbf{U}) \tag{5}$$

Equations (6)–(9) specify the arrays of conserved variables ( $\mathbf{U}$ ), the source vector ( $\mathbf{S}$ ), and the flux vector ( $\mathbf{F}(\mathbf{U})$ ). In these equations,  $q_x$  and  $q_y$  represent the discharge per unit width in the  $x$  and  $y$  directions, respectively, and are equivalent to  $HU$  and  $HV$ , respectively.

$$\mathbf{U} = \begin{Bmatrix} q_x \\ q_y \\ H \end{Bmatrix} \tag{6}$$

$$\mathbf{S} = \begin{Bmatrix} -gH \frac{\partial \zeta}{\partial x} - \frac{gn^2 U \sqrt{U^2 + V^2}}{H^{\frac{3}{2}}} \\ -gH \frac{\partial \zeta}{\partial y} - \frac{gn^2 V \sqrt{U^2 + V^2}}{H^{\frac{3}{2}}} \\ 0 \end{Bmatrix} \tag{7}$$

$$\mathbf{F} = (\mathbf{E}(\mathbf{U}), \mathbf{G}(\mathbf{U})) \tag{8}$$

$$\mathbf{E}(\mathbf{U}) = \begin{Bmatrix} \frac{q_x^2}{H} \\ \frac{q_x q_y}{H} \\ q_x \end{Bmatrix}, \mathbf{G}(\mathbf{U}) = \begin{Bmatrix} \frac{q_x q_y}{H} \\ \frac{q_y^2}{H} \\ q_y \end{Bmatrix} \tag{9}$$

By multiplying conservative Equation (5) by a shape function ( $\varphi$ ), then integrating it over an element ( $\Omega_e$ ), the discontinuous Galerkin formulation in Equation (10) is obtained. In this equation, the Gaussian theorem is applied to the flux term ( $\mathbf{F}$ ), with  $\mathbf{n} = (n_x, n_y)$  being the outward unit normal vector at an element boundary ( $\Gamma_e$ ).

$$\int_{\Omega_e} \varphi \frac{\partial \mathbf{U}}{\partial t} d\Omega + \int_{\Gamma_e} \varphi \mathbf{F} \times \mathbf{n} d\Gamma - \int_{\Omega_e} \mathbf{F} \cdot \nabla \varphi d\Omega = \int_{\Omega_e} \varphi \mathbf{S} d\Omega \tag{10}$$

The variable vector ( $\mathbf{U}$ ) is estimated over a quadrilateral element as follows:

$$\mathbf{U}(x, y) \approx \sum_{j=1}^4 U_j \varphi_j(x, y) \tag{11}$$

In Equation (11),  $U_j$  represents the value of the variables in a specific node, and  $\varphi_j(x, y)$  denotes a bilinear approximation function of the solution variables, otherwise known as a shape function. In the context of discontinuous Galerkin methods, it is permissible to allow for discontinuities in variables at the boundaries of elements. Consequently, the intercell flux is considered a function of the values ( $\mathbf{U}$ ) present within each of the two adjacent elements. Therefore, the normal flux ( $\mathbf{F} \cdot \mathbf{n}$ ) is not uniquely determined; instead, it is replaced by a numerical flux ( $\tilde{\mathbf{F}}(\mathbf{U}_L, \mathbf{U}_R)$ ), with  $\mathbf{U}_L$  being the variable at the left side (internal) of the element boundary and  $\mathbf{U}_R$  being the variable at the right side (external) of the element boundary in the counterclockwise direction. Accordingly, the second integral in Equation (10) is expressed as follows:

$$\int_{\Gamma_e} \varphi \mathbf{F} \cdot \mathbf{n} \, d\Gamma = \int_{\Gamma_e} \varphi \tilde{\mathbf{F}} \, d\Gamma \tag{12}$$

where  $\tilde{\mathbf{F}}$  is the Harten–Lax–van Leer (HLL) numerical flux. The initial step of the solution process culminates with the preliminary calculation of the conserved variables ( $q_x$  and  $q_y$ ) from Equation (10):  $\tilde{q}_x^{n+1}$  and  $\tilde{q}_y^{n+1}$ .

The non-hydrostatic pressures ( $q_b^{n+1}$ ) are obtained by a Poisson equation built and resolved by a continuous Galerkin method. The Poisson equation is derived by utilizing continuity Equation (3), vertical momentum Equation (4), and the residual portions of horizontal momentum Equations (1) and (2), incorporating the non-hydrostatic pressure terms:

$$\begin{aligned} \frac{\partial HU}{\partial t} &= -\frac{H}{2\rho} \frac{\partial q_b}{\partial x} - \frac{q_b}{2\rho} \frac{\partial(\xi - h)}{\partial x} \\ \frac{\partial HV}{\partial t} &= -\frac{H}{2\rho} \frac{\partial q_b}{\partial y} - \frac{q_b}{2\rho} \frac{\partial(\xi - h)}{\partial y} \end{aligned} \tag{13}$$

After determining the non-hydrostatic pressures ( $q_b^{n+1}$ ), Equation (13) is solved on an element to derive the ultimate solutions for discharges  $q_x^{n+1}$  and  $q_y^{n+1}$  using the following Galerkin finite-element model:

$$\begin{aligned} \int_{\Omega_e} \varphi q_x^{n+1} \, d\Omega &= \int_{\Omega_e} \varphi \tilde{q}_x^{n+1} \, d\Omega - \int_{\Omega_e} \varphi \frac{\Delta t H^n}{2\rho} \frac{\partial q_b^{n+1}}{\partial x} \, d\Omega - \int_{\Omega_e} \varphi \frac{\Delta t q_b^{n+1}}{2\rho} \frac{\partial(\xi^n - h)}{\partial x} \, d\Omega \\ \int_{\Omega_e} \varphi q_y^{n+1} \, d\Omega &= \int_{\Omega_e} \varphi \tilde{q}_y^{n+1} \, d\Omega - \int_{\Omega_e} \varphi \frac{\Delta t H^n}{2\rho} \frac{\partial q_b^{n+1}}{\partial y} \, d\Omega - \int_{\Omega_e} \varphi \frac{\Delta t q_b^{n+1}}{2\rho} \frac{\partial(\xi^n - h)}{\partial y} \, d\Omega \end{aligned} \tag{14}$$

Finally, with discharges  $q_x^n$ ,  $q_y^n$ ,  $q_x^{n+1}$ , and  $q_y^{n+1}$  and the depth ( $H^n$ ) resolved, the unresolved flow depth ( $H^{n+1}$ ) is found in continuity Equation (3) utilizing the discontinuous Galerkin expression in Equation (10). A comprehensive overview of the solution process can be found in [7].

Contrary to the earlier non-hydrostatic models, in which the non-hydrostatic pressure was resolved at the bottom, the new model consists exclusively of depth-averaged values. In order to close the system, a relation between the depth-averaged, non-hydrostatic pressure, denoted by  $q$ , and the non-hydrostatic pressure at the bottom, denoted by  $q_b$ , must be constructed. Under the assumption of a linear, non-hydrostatic pressure profile, the pressure at the bottom is twice the depth-averaged pressure:

$$q_b = 2q \tag{15}$$

Therefore, governing Equations (1)–(4), expressed using depth-averaged variables, can be written as follows:

$$\frac{\partial HU}{\partial t} + \frac{\partial HUU}{\partial x} + \frac{\partial HUV}{\partial y} = -gH \frac{\partial \xi}{\partial x} - \frac{g n^2 U \sqrt{U^2 + V^2}}{H^{\frac{1}{3}}} - \frac{1}{\rho} \left( \frac{\partial Hq}{\partial x} - 2q \frac{\partial h}{\partial x} \right) \tag{16}$$

$$\frac{\partial HV}{\partial t} + \frac{\partial HUV}{\partial x} + \frac{\partial HVV}{\partial y} = -gH \frac{\partial \zeta}{\partial y} - \frac{gn^2 V \sqrt{U^2 + V^2}}{H^{\frac{1}{3}}} - \frac{1}{\rho} \left( \frac{\partial Hq}{\partial y} - 2q \frac{\partial h}{\partial y} \right) \tag{17}$$

$$\frac{\partial H}{\partial t} + \frac{\partial UH}{\partial x} + \frac{\partial VH}{\partial y} = 0 \tag{18}$$

$$\frac{\partial W}{\partial t} + U \frac{\partial W}{\partial x} + V \frac{\partial W}{\partial y} = \frac{2q}{\rho H} \tag{19}$$

where terms  $U \frac{\partial W}{\partial x}$  and  $V \frac{\partial W}{\partial y}$  are now included in vertical momentum Equation (19). The linear assumption can be replaced by the quadratic vertical pressure profile introduced by Jeschke et al. [9], as shown in Equation (20).

$$q_b = \frac{3}{2}q + \frac{1}{4}\rho H\phi \tag{20}$$

$$\phi = -\nabla h \cdot \left( \frac{\partial \mathbf{u}}{\partial t} + (\mathbf{u} \cdot \nabla) \mathbf{u} \right) - \mathbf{u} \cdot \nabla (\nabla h) \cdot \mathbf{u} \tag{21}$$

In this work, the non-hydrostatic pressure at the bottom is considered as follows:

$$q_b = 2q\Theta + (1 - \Theta) \left( \frac{3}{2}q + \frac{1}{4}\rho H\phi \right) = \left( \frac{3}{2} + \frac{\Theta}{2} \right) q + (1 - \Theta) \frac{1}{4}\rho H\phi \tag{22}$$

Assuming  $\Theta = 1$ , the linear, non-hydrostatic pressure profile (Equation (15)) is obtained, while setting  $\Theta = 0$  yields the quadratic non-hydrostatic pressure profile (Equation (20)). Any value of  $0 < \Theta < 1$  results in a weighted average linear/quadratic non-hydrostatic pressure profile. Subsequent to the aforementioned assumption (Equation (22)), the governing equations with depth-averaged variables take the following form:

$$\frac{\partial HU}{\partial t} + \frac{\partial HUU}{\partial x} + \frac{\partial HUV}{\partial y} = -gH \frac{\partial \zeta}{\partial x} - \frac{gn^2 U \sqrt{U^2 + V^2}}{H^{\frac{1}{3}}} - \frac{1}{\rho} \left( \frac{\partial Hq}{\partial x} - \left\{ 2q\Theta + (1 - \Theta) \left( \frac{3}{2}q + \frac{1}{4}\rho H\phi \right) \right\} \frac{\partial h}{\partial x} \right) \tag{23}$$

$$\frac{\partial HV}{\partial t} + \frac{\partial HUV}{\partial x} + \frac{\partial HVV}{\partial y} = -gH \frac{\partial \zeta}{\partial y} - \frac{gn^2 V \sqrt{U^2 + V^2}}{H^{\frac{1}{3}}} - \frac{1}{\rho} \left( \frac{\partial Hq}{\partial y} - \left\{ 2q\Theta + (1 - \Theta) \left( \frac{3}{2}q + \frac{1}{4}\rho H\phi \right) \right\} \frac{\partial h}{\partial y} \right) \tag{24}$$

$$\frac{\partial H}{\partial t} + \frac{\partial UH}{\partial x} + \frac{\partial VH}{\partial y} = 0 \tag{25}$$

$$\frac{\partial W}{\partial t} + U \frac{\partial W}{\partial x} + V \frac{\partial W}{\partial y} = \frac{1}{\rho H} \left\{ 2q\Theta + (1 - \Theta) \left( \frac{3}{2}q + \frac{1}{4}\rho H\phi \right) \right\} \tag{26}$$

where the value of  $\Theta$  defines the non-hydrostatic pressure profile, which can be linear, quadratic, or weighted average linear/quadratic.

Governing Equations (23)–(26) are solved similarly to the previous model presented by Calvo et al. [7] with a linear vertical pressure profile. The solution process is described as follows:

- Solve horizontal momentum Equations (23) and (24), excluding the non-hydrostatic pressure terms by employing a discontinuous Galerkin method. The initial phase of the solution process culminates in the preliminary estimation of the conserved variables ( $q_x$  and  $q_y$ ) from Equation (10):  $\tilde{q}_x^{n+1}$  and  $\tilde{q}_y^{n+1}$ . This step is identical to the previous model.
- Find the nodal values of  $\phi$  using a continuous Galerkin solution of Equation (21).
- Using the nodal values of  $\phi$  from the previous step, the continuity Equation (25), the vertical momentum Equation (26), the kinematic boundary conditions, and the residual portion of horizontal momentum Equations (23)–(24) with the non-hydrostatic pressure parts:

$$\begin{aligned} \frac{\partial HU}{\partial t} &= -\frac{1}{\rho} \left( \frac{\partial Hq}{\partial x} - \left\{ 2q\Theta + (1 - \Theta) \left( \frac{3}{2}q + \frac{1}{4}\rho H\phi \right) \right\} \frac{\partial h}{\partial x} \right) \\ \frac{\partial HV}{\partial t} &= -\frac{1}{\rho} \left( \frac{\partial Hq}{\partial y} - \left\{ 2q\Theta + (1 - \Theta) \left( \frac{3}{2}q + \frac{1}{4}\rho H\phi \right) \right\} \frac{\partial h}{\partial y} \right) \end{aligned} \tag{27}$$

construct a Poisson equation that is resolved by a continuous Galerkin method to find the non-hydrostatic pressures ( $q^{n+1}$ ).

- With the non-hydrostatic pressures ( $q^{n+1}$ ) determined, Equation (27) is resolved on an element to obtain the final discharges ( $q_x^{n+1}$  and  $q_y^{n+1}$ ).
- Lastly, with discharges  $q_x^n$ ,  $q_y^n$ ,  $q_x^{n+1}$ , and  $q_y^{n+1}$  and the depth ( $H^n$ ) known, the unresolved depth ( $H^{n+1}$ ) is found from continuity Equation (25) using the discontinuous Galerkin expression in Equation (10). This step is identical to the previous model.

### 3. Linear Dispersion

The linear dispersion relation of depth-averaged Equations (23)–(26), for the one-dimensional case, without friction and assuming a constant bathymetry, is expressed as follows [11]:

$$\omega_{nh,weight}^2 = \frac{c_{sw}^2 k^2}{1 + \frac{(kh)^2}{2(\frac{3}{2} + \frac{\Theta}{2})}} \tag{28}$$

where  $\omega_{nh,weight}$  is the wave frequency of the non-hydrostatic model using the weighted average pressure profile,  $c_{sw} = \sqrt{gh}$  is the shallow-water wave speed, and  $k = \frac{2\pi}{\lambda}$  is the wave number. Using  $\Theta = 1$ , the linear, non-hydrostatic pressure profile is applied, leading to the following dispersion relation:

$$\omega_{nh,lin}^2 = \frac{c_{sw}^2 k^2}{1 + \frac{(kh)^2}{4}} \tag{29}$$

whereas, using  $\Theta = 0$ , the quadratic non-hydrostatic pressure profile is applied, leading to the following dispersion relation:

$$\omega_{nh,quad}^2 = \frac{c_{sw}^2 k^2}{1 + \frac{(kh)^2}{3}} \tag{30}$$

These same results were reported by Cui et al. [13] for the linear vertical profile and by Aïssiouene [14] for both profiles. On the other hand, the dispersion relation derived from the full linearized equations of Airy wave theory is expressed as follows:

$$\omega_{nh,full}^2 = gk \tanh(kh) \tag{31}$$

These dispersion relations are used to ensure the accuracy of the numerical results. From Equations (28) and (31), we obtain an expression for  $\Theta$  that yields the dispersion relation of the full linearized equations:

$$\Theta = \frac{3kh - (3 + (kh)^2) \tanh(kh)}{\tanh(kh) - kh} \tag{32}$$

The above equation for  $\Theta$ , which gives the dispersion relation of the linearized equations (Equation (31)), depends on  $k = \frac{2\pi}{\lambda}$  and the depth ( $h$ ). The wavelength ( $\lambda$ ) is provided by Airy’s linear theory:

$$\lambda = \frac{gT^2}{2\pi} \tanh\left(\frac{2\pi}{\lambda}\right) \tag{33}$$

An explicit formula for the calculation of  $\lambda$  and, subsequently,  $\Theta$  is the approximation of Fenton and McKee [15]:

$$\lambda = \frac{gT^2}{2\pi} \left( \tanh \left[ \frac{2\pi \sqrt{\frac{h}{g}}}{T} \right]^{\frac{3}{2}} \right)^{\frac{2}{3}} \tag{34}$$

This approximation produces a maximum error of 2% for shallow, intermediate, and deep depths and can be used to determine  $\Theta$  from Equation (32).

### 4. Model Validation

Model validation was performed using the analytical solution of a linear standing wave in one spatial dimension with constant bathymetry:

$$H(x, t) = h - a \sin(kx) \cos(kct) \tag{35}$$

$$HU(x, t) = accos(kx) \sin(kct) \tag{36}$$

with  $a$  being the wave amplitude and  $c$  the wave phase speed.

The numerical model was applied on a computational domain length equal to one wavelength. The periodic boundary conditions of Equation (36) were imposed at each end of the numerical domain. The water depth ( $h$ ) was varied, while the wavelength and the wave amplitude were held constant at  $\lambda = \frac{2\pi}{k} = 20$  m and  $a = 0.01$  m, respectively. This was done to obtain ratios for  $\frac{h}{\lambda}$  between 0.05 and 1.0 and ratios for  $\frac{a}{h}$  between 0.01 and 0.005. The computational domain was discretized with a quadrilateral element mesh with sides of  $\Delta x = \Delta y = 5$  cm. The simulation time was one wave period.

Figure 1 displays the normalized phase velocities resulting from applying non-hydrostatic Equations (23)–(26) with either the linear ( $\Theta = 1$ ), the quadratic ( $\Theta = 0$ ), or the weighted average linear/quadratic ( $\Theta = f(kh)$ ) vertical pressure. Additionally, they were compared to their analytical phase velocities obtained from Equations (29) and (30) and the full reference-phase velocity obtained from Equation (31). All numerical dispersion relations were found to be in exact agreement with their analytical counterparts, highlighting the case of the full linearized equations and non-hydrostatic Equations (23)–(26) where the values of  $\Theta = f(kh)$  were calculated by Equation (32).

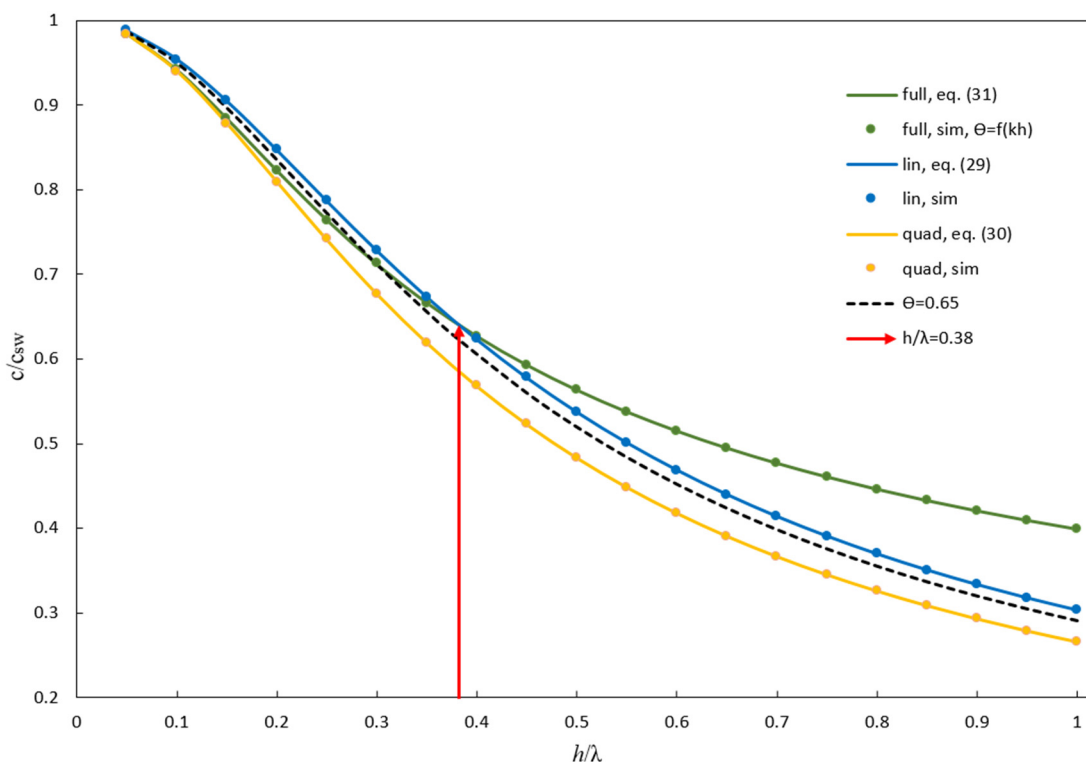


**Figure 1.** Periodic standing wave: simulated non-hydrostatic phase velocities and analytic reference values.

In the application of Equations (23)–(26) to the cases of variable bathymetry, only values of  $\Theta$  calculated by Equation (32) in the interval of  $0 \leq \frac{h}{\lambda} \leq 0.38$  were used (Figure 1). This is because averaging must occur within the limits of the two models (quadratic and linear;  $0 \leq \Theta \leq 1$ ) whose applicability is being verified. The value of  $\Theta$  that minimizes the sum of the absolute deviations from the full Airy wave-theory phase velocity in the range of  $0 \leq \frac{h}{\lambda} \leq 0.38$  is  $\Theta = 0.65$ , as shown in Figure 1.

Figure 2 shows a time series of the surface elevation for the linear, quadratic, and weighted average linear/quadratic ( $\Theta = 1.58$ ) vertical pressure profiles evaluated at  $x = 5$  m. The simulation time is 25 s, and the ratio of depth to wavelength is 0.5. As shown in Figure 2, the linear and quadratic pressure profiles lag behind the analytical solution—in particular, the quadratic profile—while the weighted average linear/quadratic pressure profile can precisely reproduce the evolution of the water height.

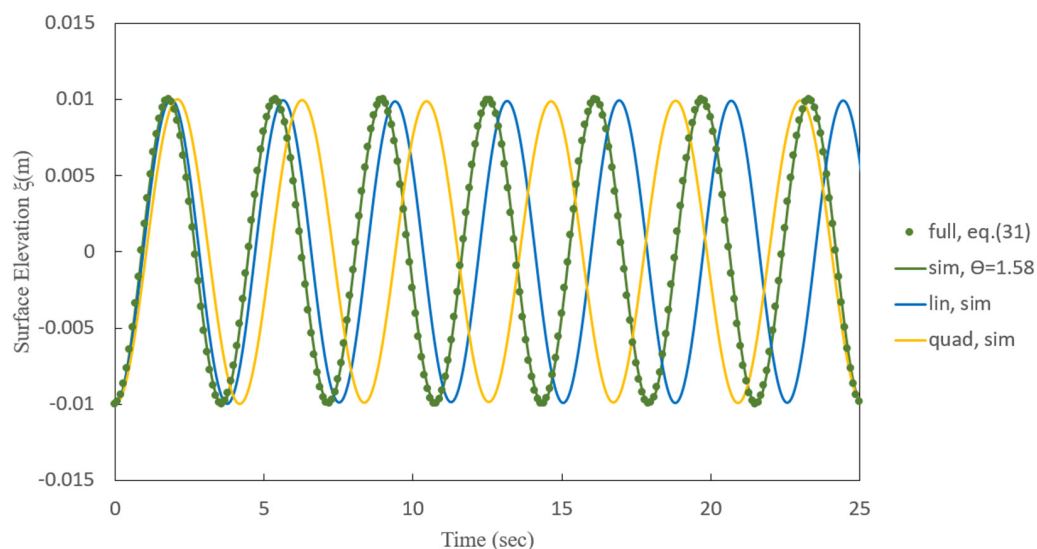


**Figure 2.** Periodic standing wave: simulated (green, blue, and yellow lines) and analytical (green dots) surface elevation with linear, quadratic, and weighted average linear/quadratic vertical profiles. Simulation time = 25 s,  $x = 5$  m, and  $\frac{h}{\lambda} = 0.5$ .

### 5. Beji and Battjes’ Experiment of Wave Propagation on a Submerged Bar

Beji and Battjes [16] conducted physical experiments on the propagation of waves over a submerged trapezoidal bar. The channel utilized in the experiments had a length of 37.7 m, a depth of 0.75 m, and a width of 0.8 m.

The numerical configuration of the experiment is shown in Figure 3. The still water depth is 0.4 m. The trapezoidal bar had a height of 0.3 m, with a slope of 1:20 on the front side and 1:10 on the back side. Incident sinusoidal waves with  $a = 1.0$  cm and  $T = 2.02$  s, corresponding to  $kh = 0.67$  ( $\frac{h}{\lambda} = 0.11$ ), were imposed on the left side of the channel. A Sommerfeld radiation condition was applied to the right side. The non-hydrostatic pressure ( $q_b$ ) was taken as zero on both the left and right sides of the channel. The computational domain measures 35 m in length and was discretized with a quadrilateral element mesh with sides measuring 1.25 cm. At the start of the simulation, the velocity and water surface elevation were set to zero, and a short time interval of  $\Delta t = 0.002$  s was used to develop the wave smoothly.

Figure 4 compares simulated elevations with free surface measurements recorded at points 8, 9, 10, and 11 in Figure 3. As illustrated in Figure 4, the weighted average linear/quadratic profile using  $\Theta = 0.65$  improves the comparisons between measured and simulated wave elevations at all four measurement points.

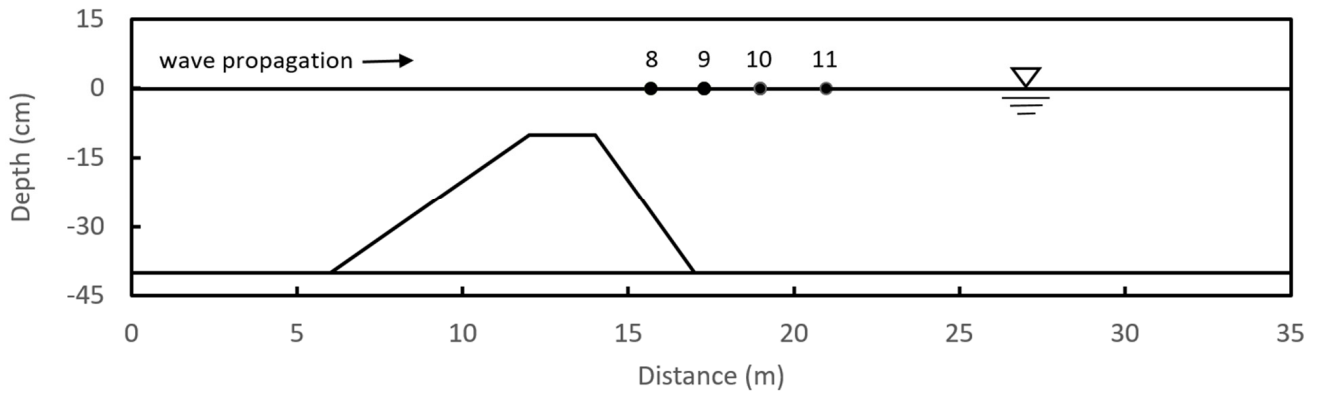


**Figure 3.** Numerical configuration for Beji and Battjes’ [16] experiment on wave propagation over a bar.

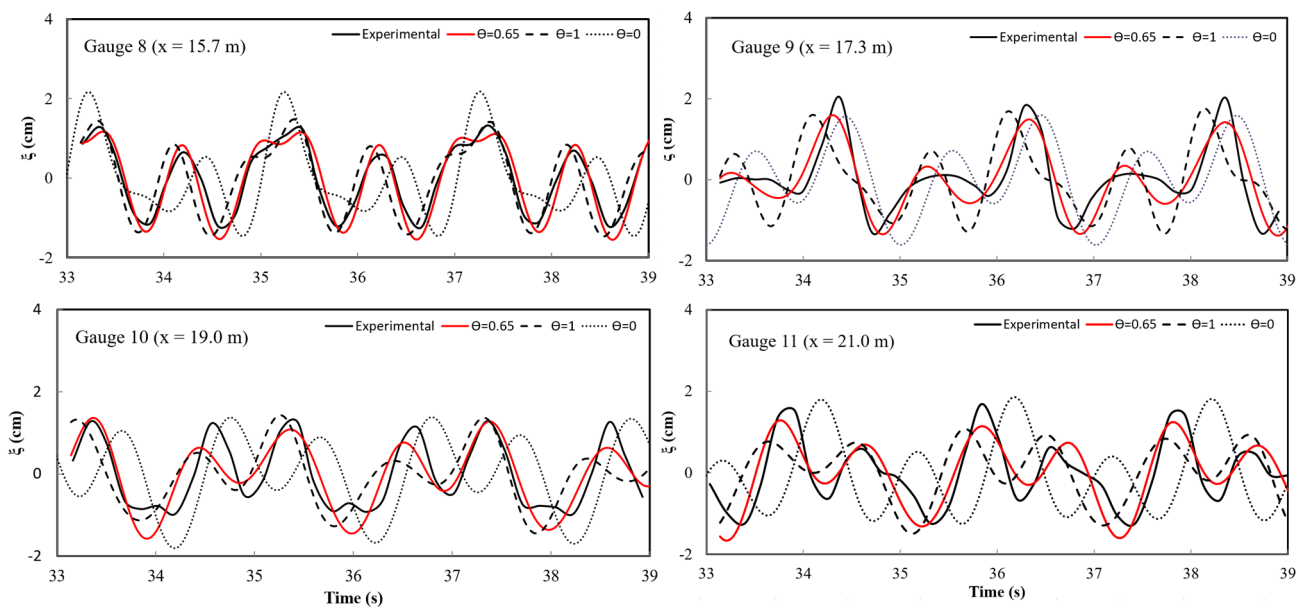


**Figure 4.** Simulated elevations and free surface measurements for Beji and Battjes’ [16] experiment for the case of wave propagation over a submerged bar. Experiment (black line); linear/quadratic profile:  $\Theta = 0.65$  (red line); linear profile:  $\Theta = 1$  (dashed line); quadratic profile:  $\Theta = 0$  (dotted line).

The Wilmott index [17] was used to quantify the correspondence between the simulated and observed free surface elevations in Figure 4. The Wilmott index is a normalized metric that quantifies the degree of concordance between observed and simulated values. A Wilmott index value of 1 indicates perfect agreement, expressed as follows:

$$I_w = 1 - \frac{\sum_{i=1}^n (X_{c_i} - X_{m_i})^2}{\sum_{i=1}^n [ |X_{c_i} - \bar{X}_m| + |X_{m_i} - \bar{X}_m| ]^2} \tag{37}$$

where  $X_{c_i}$  and  $X_{m_i}$  are the simulated and measured values, respectively. The bar denotes the average of the measured values, and  $n$  is the number of measurements.

Table 1 lists the Wilmott index values ( $I_w$ ) from Beji and Battjes’ laboratory experiments for gauges 8, 9, 10, and 11 in Figure 4. The table shows that higher  $I_w$  values (bold values in Table 1) for each gauge are obtained using the weighted average linear/quadratic profile with  $\Theta = 0.65$ .

**Table 1.** Values of  $I_w$  for Beji and Battjes’ laboratory experiments: gauges 8 to 11.

	Gauge 8	Gauge 9	Gauge 10	Gauge 11
$\Theta = 0.65$	0.98	0.94	0.92	0.93
$\Theta = 1$	0.94	0.66	0.81	0.71
$\Theta = 0$	0.74	0.73	0.57	0.21

### 6. Whalin’s Wave Diffraction Experiment on a Semicircular Shoal and Comparison with Experimental Data

Whalin [18] conducted a series of laboratory experiments with the objective of studying the wave refraction and focusing phenomenon caused by a semicircular sloping bathymetry. This has become a standard benchmark for the validation of dispersive numerical models used to test nonlinear refraction and diffraction, primarily using higher-order Boussinesq-type models [19–22] or multi-layer, non-hydrostatic models [23]. The experiments were conducted in a wave tank with a length of 25.603 m and a width of 6.096 m (Figure 5). The initial water depth was 0.4572 m. In the central segment ( $7.622 \text{ m} \leq x^* \leq 15.242 \text{ m}$ ) eleven regularly spaced semicircular steps led to the shallowest part, where the water depth was 0.1524 m [22,23].

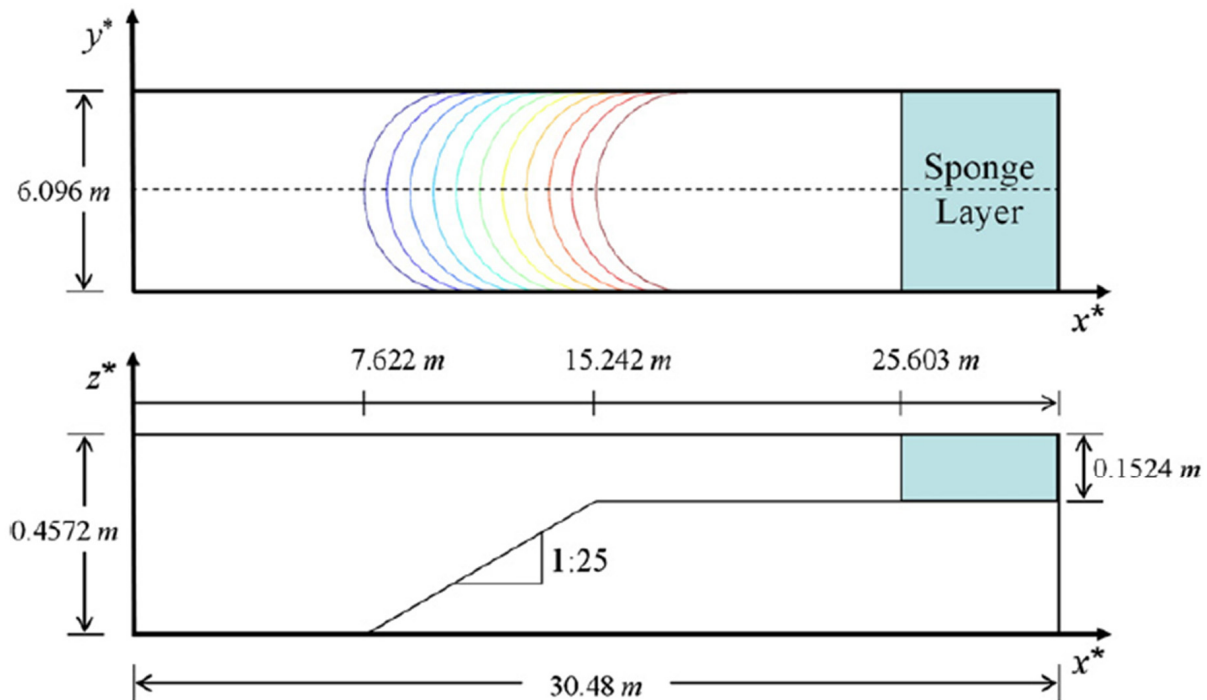


**Figure 5.** Bottom configuration for wave propagation over a semicircular shoal used in the experiments of Whalin [18] (Source: [23]).

The bathymetry was symmetrical to the tank centerline at  $y^* = 3.048 \text{ m}$  and described as follows:

$$h(x^*, y^*) = \begin{cases} 0.4572 & 0 \leq x^* \leq 10.67 - G \\ \frac{(0.4572 + 10.67 - G)}{25} & 10.67 - G \leq x^* \leq 18.29 - G \\ 0.1542 x^* & 18.29 - G \leq x^* \leq 25.603 \end{cases}$$

$$G(y^*) = \sqrt{y^*(6.096 - y^*)} \tag{38}$$

where  $x^*$  and  $y^*$  refer to length variables, measured in meters.

Three series of numerical computations were performed to produce waves of varying periods ( $T$ ) and wave amplitudes ( $a$ ).

Case I:  $T = 3.0 \text{ s}$ ,  $a = 0.0068 \text{ m}$ ,  $\left(\frac{h}{\lambda} = 0.07\right)$ ;

Case II:  $T = 2.0 \text{ s}$ ,  $a = 0.0075 \text{ m}$ ,  $\left(\frac{h}{\lambda} = 0.12\right)$ ;

Case III:  $T = 1.0 \text{ s}$ ,  $a = 0.0195 \text{ m}$ ,  $\left(\frac{h}{\lambda} = 0.31\right)$ .

An incoming periodic wave train was generated in a 5 m generation zone. Sponge layers were applied in the upstream and downstream directions, with the primary function of absorbing outward and reflected waves. In addition, solid wall conditions were implemented at the lateral boundaries. A mesh with  $\Delta x = 5 \text{ cm}$  and  $\Delta y = 10 \text{ cm}$  was used for the case I and II tests. For the test in case III,  $\Delta x = 2.5 \text{ cm}$  and  $\Delta y = 10 \text{ cm}$  were used, as this was the most intense case. Wave propagation was simulated for 100 s, and numerical data were obtained for the last 25 s. Subsequent to the measurement of water surface elevation along the center of the shoal, a harmonic analysis was conducted to ascertain the amplitude of the frequencies. The surface elevation time series along the centerline was subjected to analysis to obtain the amplitudes of the first, second, and third harmonics. Figures 6–8 present the comparisons between the numerical results and the experimental data. These simulations also tested the utilization of the  $\Theta$  parameter calculated using Equation (32), with the wavelength ( $\lambda$ ) calculated according to Equation (34).

For case I, some disparities were observed between the numerical outputs and the experimental data (Figure 6). Similar results were observed in preceding studies [19–21], usually attributed to reflected waves in the experiments.

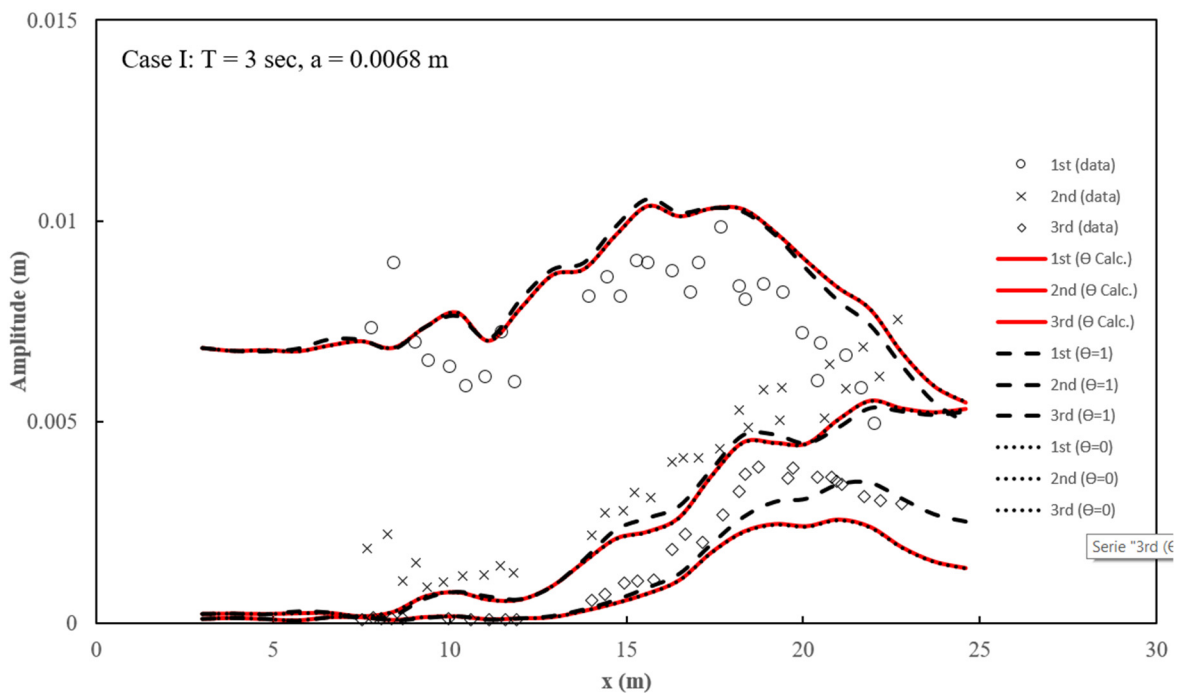


**Figure 6.** Waves over a semicircular shoal (case I): comparison of simulated and experimental wave amplitudes of harmonics 1, 2, and 3 along the centerline. Experiment (circles); linear/quadratic profile:  $\Theta$  calculated by Equation (32) (red line); linear profile:  $\Theta = 1$  (dashed line); quadratic profile:  $\Theta = 0$  (dotted line).

In case II, considerable improvements are observed in the comparisons between observed and simulated harmonics using the  $\Theta$  parameter calculated according to Equations (32) and (34) (red lines in Figure 7).

For case III (Figure 8), the relatively high  $\frac{h}{\lambda} = 0.31$  ratio of the incident wave leads to better model performance using  $\Theta = 1$  (linear, non-hydrostatic pressure profile), particularly at the end of the ramp ( $x > 15 \text{ m}$ ). This could be because wave shoaling decreases the

wavelength ( $\lambda$ ), resulting in a further increase in  $\frac{h}{\lambda}$ , in addition to the wave's nonlinearity in this zone.

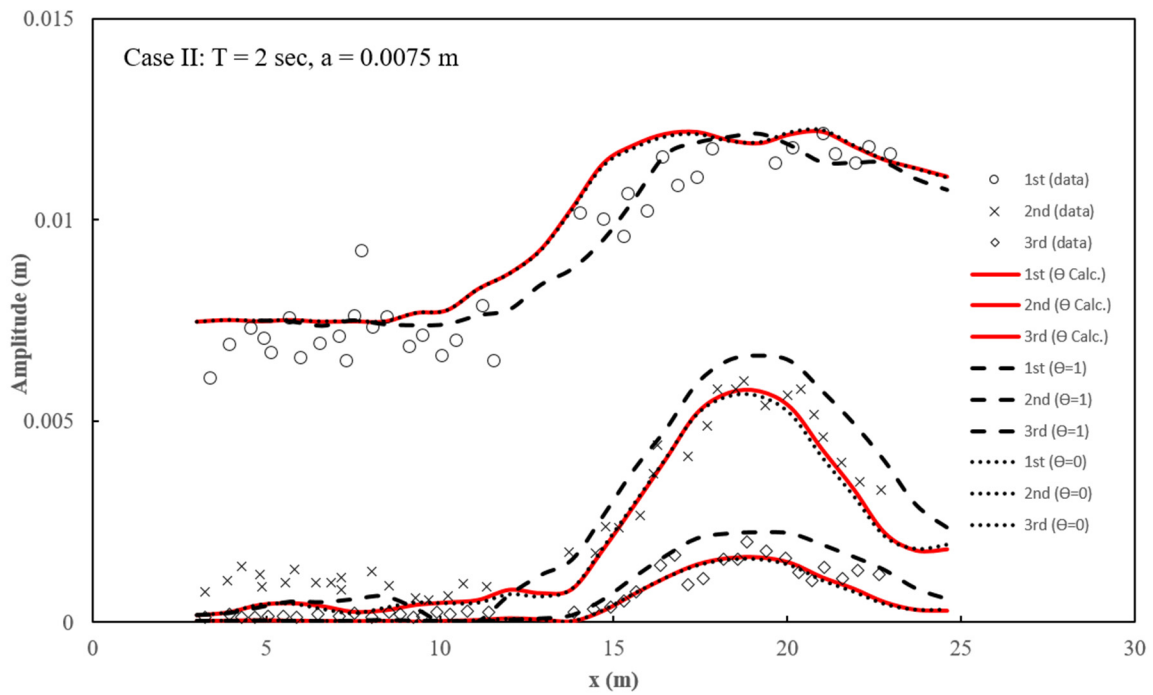


**Figure 7.** Waves over a semicircular shoal (case II): comparison of simulated and experimental wave amplitudes of harmonics 1, 2, and 3 along the centerline. Experiment (circles); linear/quadratic profile:  $\Theta$  calculated by Equation (32) (red line); linear profile:  $\Theta = 1$  (dashed line); quadratic profile:  $\Theta = 0$  (dotted line).

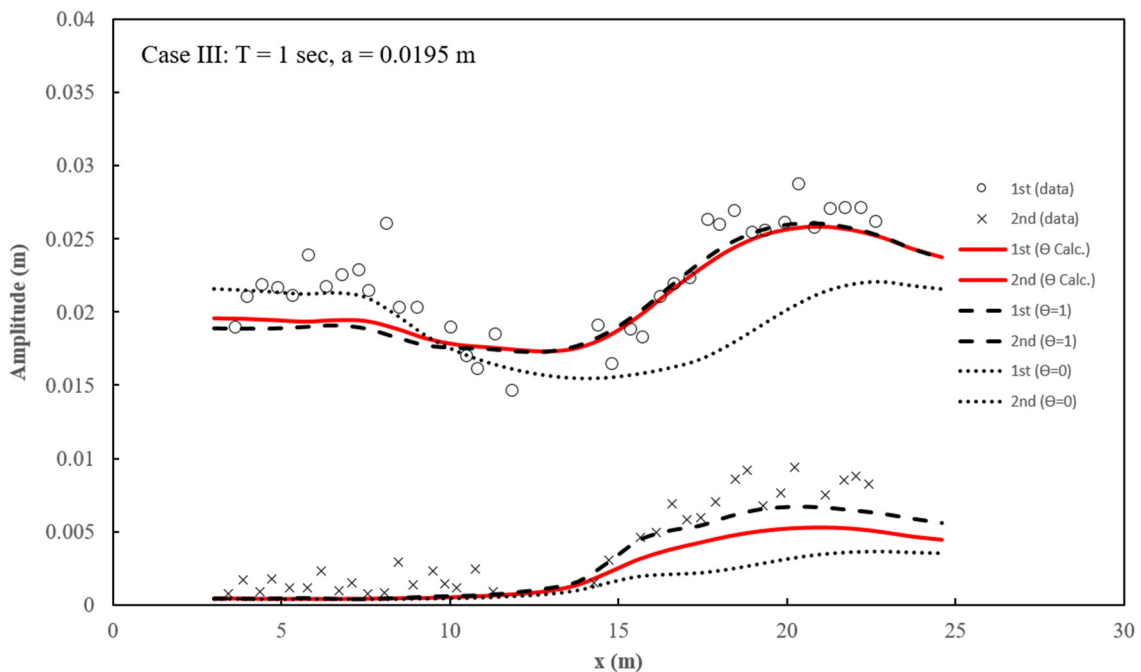


**Figure 8.** Waves over a semicircular shoal (case III): comparison of simulated and experimental wave amplitudes of harmonics 1 and 2 along the centerline. Experiment (circles); linear/quadratic profile:  $\Theta$  calculated by Equation (32) (red line); linear profile:  $\Theta = 1$  (dashed line); quadratic profile:  $\Theta = 0$  (dotted line).

Table 2 presents the values of  $I_w$  from Whalin’s laboratory experiments for cases I to III and for the first, second, and third harmonics. For case I, the linear profile ( $\Theta = 1$ ) had the higher  $I_w$  values. The comparatively reduced  $I_w$  values observed in the first and third harmonics can be attributed to reflected waves occurring during the experimental procedure. In case II, the  $\Theta$  parameter calculated using Equations (32) and (34) resulted in higher  $I_w$  values for all three harmonics, while high  $I_w$  values were also achieved with the quadratic profile ( $\Theta = 0$ ). For case III, the  $\Theta$  parameter calculated using Equations (32) and (34) yielded a higher  $I_w$  value for the first harmonic, while the linear profile achieved a higher  $I_w$  value for the second harmonic.

Table 2. Values of  $I_w$  from Whalin’s laboratory experiments: cases I to III.

	Case I			Case II			Case III	
	1st	2nd	3rd	1st	2nd	3rd	1st	2nd
$\Theta$ Calc.	0.68	<b>0.98</b>	0.63	<b>0.95</b>	<b>0.98</b>	<b>0.97</b>	<b>0.89</b>	0.85
$\Theta = 1$	<b>0.70</b>	<b>0.98</b>	<b>0.70</b>	0.94	0.97	0.93	0.88	<b>0.94</b>
$\Theta = 0$	0.68	<b>0.98</b>	0.63	<b>0.95</b>	<b>0.98</b>	0.96	0.61	0.66

### 7. Wave Transformation over an Elliptic Shoal

The transformation of waves over a submerged elliptical shoal is a standard example employed in evaluating non-hydrostatic models to simulate wave refraction, diffraction, and focusing. Non-hydrostatic 3D models have been demonstrated to accurately simulate wave propagation in this case by employing a multigrid solver [24] or a limited number of vertical layers [3,4,25].

Figure 9 shows the setup of the experiment conducted by Vincent and Briggs [26], featuring an elliptical shoal. The boundary of the shoal can be described as follows:

$$\left(\frac{x}{3.05}\right)^2 + \left(\frac{y}{3.96}\right)^2 = 1 \tag{39}$$

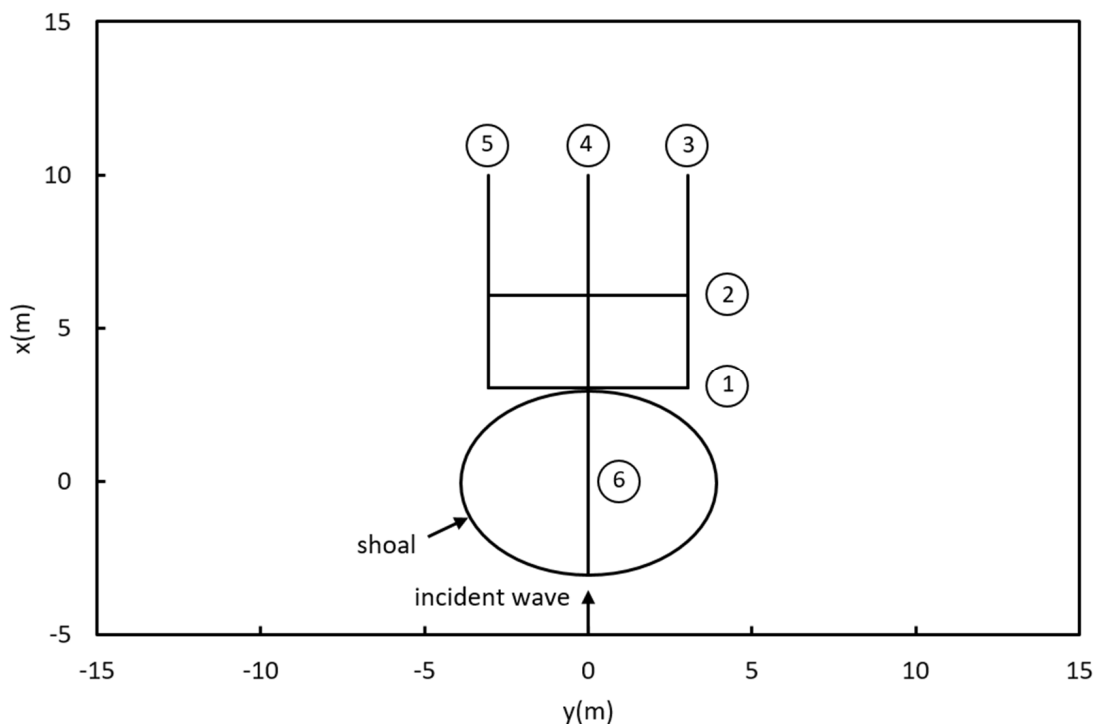


Figure 9. Schematic of Vincent and Briggs’ [26] experimental setup and measurement sections.

The depth over the elliptical shoal ( $h_e$ ) is expressed as follows:

$$h_e = 0.9144 - 0.762 \sqrt{1 - \left(\frac{x}{3.81}\right)^2 - \left(\frac{y}{4.95}\right)^2} \tag{40}$$

The constant water depth outside the elliptical shoal zone was  $h_0 = 0.457$  m. A comprehensive investigation encompassed 17 incoming wave situations, ranging from non-breaking waves to breaking waves from different directions. Surface elevations were recorded at the six cross-sections depicted in Figure 9. In the model simulations, a non-breaking incoming wave situation was employed. At the incoming boundary, a wave with a height of  $H_0 = 2.54$  cm and period of  $T = 1.3$  s was applied, corresponding to a ratio of  $\frac{h}{\lambda} = 0.2$ . At the outgoing boundary, a 5 m absorption zone dissipated outbound waves. The boundary conditions of impermeability and free slip were applied to the side walls. A mesh with  $\Delta x = 5$  cm and  $\Delta y = 10$  cm was used to discretize the numerical domain.

Figure 10 shows how the model’s results in comparison with the measured data on wave height normalized with respect to the initial height ( $H/H_0$ ) at the cross sections shown in Figure 9. The wave height was calculated by taking the arithmetic mean of the wave heights over five stable wave periods.

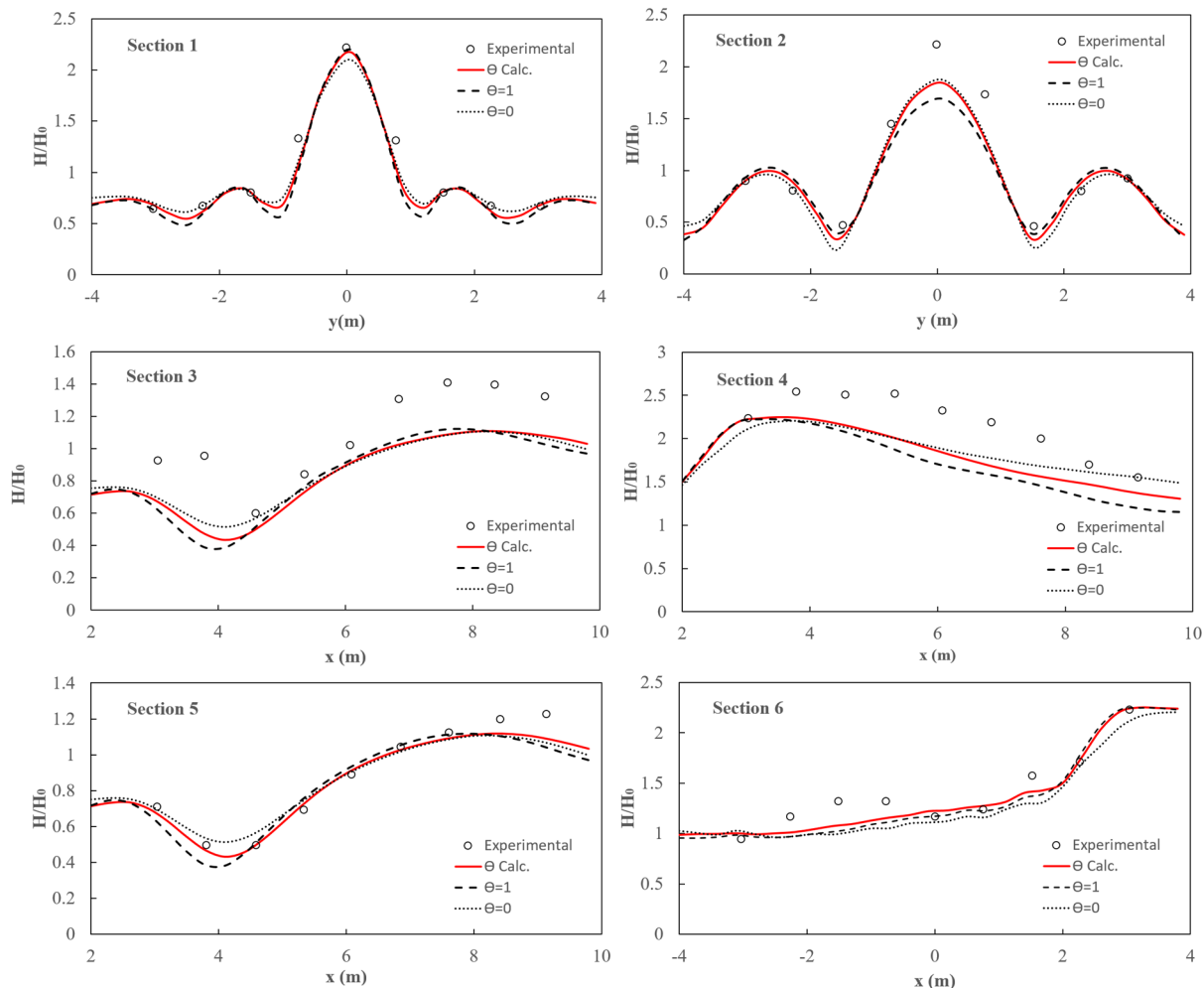


**Figure 10.** Simulated elevations and free surface measurements for Vincent and Briggs’ [26] experiment on waves over an elliptic shoal. Experiment (circles); linear/quadratic profile:  $\Theta$  calculated by Equation (32) (red line); linear profile:  $\Theta = 1$  (dashed line); quadratic profile:  $\Theta = 0$  (dotted line).

The models accurately predicted the wave concentration behind the bank in section 1. In section 2, the models did not reach the experimental wave height due to the limitations inherent to vertically averaged models and the dissipative characteristic of the first-order explicit temporal approximation used in non-hydrostatic models [6,27]. In sections 4 and 6, the wave was steepened along the direction of propagation, and the combination of the refracting wave fronts produced a maximum wave height around  $x = 4$  m. After this point, the wave became smaller because the wave energy moved to the sides in sections 3 and 5. Figure 10 shows that utilizing a calculated  $\Theta$  parameter generally improved comparisons between measured and simulated wave heights.

Table 3 presents the values of  $I_w$  from Vincent and Briggs' laboratory experiments for sections 1 through 6 in Figure 10. The table indicates that using a  $\Theta$  parameter calculated using Equations (32) and (34) resulted in higher  $I_w$  values in four out of six sections. Meanwhile, higher  $I_w$  values were achieved in three out of six sections when the quadratic profile ( $\Theta = 0$ ) was employed. The linear profile ( $\Theta = 1$ ) could not attain higher  $I_w$  values in any given section.

**Table 3.** Values of  $I_w$  from Vincent and Briggs' laboratory experiments: sections 1 to 6.

	Section 1	Section 2	Section 3	Section 4	Section 5	Section 6
$\Theta$ Calc.	0.98	<b>0.96</b>	0.76	<b>0.76</b>	<b>0.99</b>	<b>0.97</b>
$\Theta = 1$	0.98	0.92	0.74	0.69	0.97	0.96
$\Theta = 0$	<b>0.99</b>	<b>0.96</b>	<b>0.77</b>	0.75	0.98	0.93

## 8. Conclusions

A novel two-dimensional, depth-integrated, non-hydrostatic model was formulated for the purpose of simulating wave propagation. This model employs a weighted average linear/quadratic non-hydrostatic pressure profile. The model was established by altering the non-hydrostatic discontinuous/continuous Galerkin finite-element model with a linear vertical non-hydrostatic pressure profile described by Calvo et al. [7].

A series of numerical experiments was conducted to verify and validate the proposed model. The first case, with an analytical solution, was the simulation of a linear standing wave in one spatial dimension with constant bathymetry, which validated the model's dispersive properties. The following three sets of previous laboratory experiments conducted by other authors, representing various nearshore wave propagation phenomena (wave propagation on a submerged bar, wave diffraction on a semicircular shoal, and wave transformation over an elliptical shoal), were used to validate the model's ability to simulate nearshore waves.

The employment of a weighted average linear/quadratic non-hydrostatic pressure profile has been shown to enhance the performance of earlier models utilizing linear or quadratic non-hydrostatic pressure profiles. The findings indicate that the application of a weighted average linear/quadratic non-hydrostatic pressure profile, in conjunction with a calculated or optimized  $\Theta$  weight parameter, leads to improvement in the dispersion characteristics of depth-integrated, non-hydrostatic models, particularly in shallow and intermediate water depths.

Future work will include further analysis of the model in cases of variable bathymetry and comparisons with traditional Boussinesq-type models.

**Author Contributions:** Conceptualization, L.C., D.D.P. and M.M.; methodology, L.C.; software, L.C.; validation, L.C.; formal analysis, L.C., D.D.P. and M.M.; investigation, L.C. and D.D.P.; writing—original draft preparation, L.C.; writing—review and editing, L.C., D.D.P. and M.M.; funding acquisition, L.C. All authors have read and agreed to the published version of the manuscript.

**Funding:** This work was supported by the Sistema Nacional de Investigación (SNI), and the Dirección de Investigación Científica y Desarrollo Tecnológico (I+D) of the Secretaría Nacional de Ciencia, Tecnología e Innovación (SENACYT), Panamá.

**Data Availability Statement:** The original contributions presented in the study are included in the article, further inquiries can be directed to the corresponding author.

**Conflicts of Interest:** The authors declare no conflict of interest.

## References

1. Casulli, V.; Stelling, G.S. Numerical Simulation of 3D Quasi-Hydrostatic, Free-Surface Flows. *J. Hydraul. Eng.* **1998**, *124*, 678–686. [[CrossRef](#)]
2. Stansby, P.K.; Zhou, J.G. Shallow-water flow solver with non-hydrostatic pressure: 2D vertical plane problems. *Int. J. Numer. Methods Fluids* **1998**, *28*, 541–563. [[CrossRef](#)]
3. Stelling, G.; Zijlema, M. An accurate and efficient finite difference algorithm for non-hydrostatic free surface flow with application to wave propagation. *Int. J. Numer. Methods Fluids* **2003**, *43*, 1–23. [[CrossRef](#)]
4. Zijlema, M.; Stelling, G.S. Further experiences with computing non-hydrostatic free-surface flows involving water waves. *Int. J. Numer. Methods Fluids* **2004**, *48*, 169–197. [[CrossRef](#)]
5. Zijlema, M.; Stelling, G. Efficient computation of surf zone waves using the nonlinear shallow water equations with non-hydrostatic pressure. *Coast. Eng.* **2008**, *55*, 780–790. [[CrossRef](#)]
6. Zijlema, M.; Stelling, G.S.; Smith, P. SWASH: An operational public domain code for simulating wave fields and rapidly varied flows in coastal waters. *Coast. Eng.* **2011**, *58*, 992–1012. [[CrossRef](#)]
7. Calvo, L.; De Padova, D.; Mossa, M.; Rosman, P. Non-Hydrostatic Discontinuous/Continuous Galerkin Model for Wave Propagation, Breaking and Runup. *Computation* **2021**, *9*, 47. [[CrossRef](#)]
8. Bai, Y.; Cheung, K.F. Dispersion and nonlinearity of multi-layer non-hydrostatic free-surface flow. *J. Fluid Mech.* **2013**, *726*, 226–260. [[CrossRef](#)]
9. Jeschke, A.; Vater, S.; Behrens, J. A discontinuous Galerkin method for non-hydrostatic shallow water flows. In Proceedings of the Conference: Finite Volumes for Complex Applications VIII—Hyperbolic, Elliptic and Parabolic Problems, Lille, France, 12–16 June 2017.
10. Wang, W.; Martin, T.; Kamath, A.; Bihs, H. An improved depth-averaged non-hydrostatic shallow water model with quadratic pressure approximation. *Int. J. Numer. Methods Fluids* **2020**, *92*, 803–824. [[CrossRef](#)]
11. Jeschke, A. Second Order Convergent Discontinuous Galerkin Projection Method for Dispersive Shallow Water Flows. Ph.D. Thesis, University of Hamburg, Hamburg, Germany, 2018.
12. Wang, W.; Kamath, A.; Martin, T.; Pákozdi, C.; Bihs, H. A Comparison of Different Wave Modelling Techniques in An Open-Source Hydrodynamic Framework. *J. Mar. Sci. Eng.* **2020**, *8*, 526. [[CrossRef](#)]
13. Cui, H.; Pietrzak, J.; Stelling, G. Optimal dispersion with minimized Poisson equations for non-hydrostatic free surface flows. *Ocean Model.* **2014**, *81*, 1–12. [[CrossRef](#)]
14. Aïssiouene, N. Numerical Analysis and Discrete Approximation of a Dispersive Shallow Water Model. Ph.D. Thesis, Pierre et Marie Curie, Paris VI, Paris, France, 2016.
15. Fenton, J.; McKee, W. On calculating the lengths of water waves. *Coast. Eng.* **1990**, *14*, 499–513. [[CrossRef](#)]
16. Beji, S.; Battjes, J. Experimental investigation of wave propagation over a bar. *Coast. Eng.* **1993**, *19*, 151–162. [[CrossRef](#)]
17. Wilmott, C.J. On the validation of models. *Phys. Geogr.* **1981**, *2*, 184–194. [[CrossRef](#)]
18. Whalin, R.W. The Limit of Applicability of Linear Wave Refraction Theory in a Convergence Zone. Ph.D. Thesis, Texas A&M University, Vicksburg, MS, USA, 1971.
19. Bingham, H.B.; Madsen, P.A.; Fuhrman, D.R. Velocity potential formulations of highly accurate Boussinesq-type models. *Coast. Eng.* **2009**, *56*, 467–478. [[CrossRef](#)]
20. Tonelli, M.; Petti, M. Hybrid finite volume—Finite difference scheme for 2DH improved Boussinesq equations. *Coast. Eng.* **2009**, *56*, 609–620. [[CrossRef](#)]
21. Kazolea, M.; Delis, A.; Nikolos, I.; Synolakis, C. An unstructured finite volume numerical scheme for extended 2D Boussinesq-type equations. *Coast. Eng.* **2012**, *69*, 42–66. [[CrossRef](#)]
22. Lannes, D.; Marche, F. A new class of fully nonlinear and weakly dispersive Green–Naghdi models for efficient 2D simulations. *J. Comput. Phys.* **2015**, *282*, 238–268. [[CrossRef](#)]
23. Young, C.; Wu, C.; Liu, W.; Kuo, J. A higher-order non-hydrostatic  $\sigma$  model for simulating non-linear refraction—Diffraction of water waves. *Coast. Eng.* **2009**, *56*, 919–930. [[CrossRef](#)]
24. Li, B.; Fleming, C.A. Three-dimensional model of Navier–Stokes equations for water waves. *J. Waterway Port Coast. Ocean Eng.* **2001**, *127*, 16–25. [[CrossRef](#)]

25. Yuan, H.L.; Wu, C.H. An implicit 3D fully non-hydrostatic model for free-surface flows. *Int. J. Numer. Meth. Fluids* **2004**, *46*, 709–733. [[CrossRef](#)]
26. Vincent, C.L.; Briggs, M.J. Refraction—Diffraction of Irregular Waves over a Mound. *J. Waterw. Port Coast. Ocean Eng.* **1989**, *115*, 269–284. [[CrossRef](#)]
27. Wei, Z.; Jia, Y. Simulation of nearshore wave processes by a depth-integrated non-hydrostatic finite element model. *Coast. Eng.* **2014**, *83*, 93–107. [[CrossRef](#)]

**Disclaimer/Publisher’s Note:** The statements, opinions and data contained in all publications are solely those of the individual author(s) and contributor(s) and not of MDPI and/or the editor(s). MDPI and/or the editor(s) disclaim responsibility for any injury to people or property resulting from any ideas, methods, instructions or products referred to in the content.